Effect of the Device Architecture on the Performance of FA(0.85)MA(0.15)PbBr(0.45)I(2.55) Planar Perovskite Solar Cells

Adjokatse, Sampson; Kardula, Jane; Fang, Hong-Hua; Shao, Shuyan; ten Brink, Gert H.; Loi, Maria Antonietta

Published in:
Advanced Materials Interfaces

DOI:
10.1002/admi.201801667

Publication date:
2019

ADVANCED MATERIALS INTERFACES

www.advmatinterfaces.de

Effect of the Device Architecture on the Performance of $FA_{0.85}MA_{0.15}PbBr_{0.45}I_{2.55}$ Planar Perovskite Solar Cells

*Sampson Adjokatse, Jane Kardula, Hong-Hua Fang, Shuyan Shao, Gert H. ten Brink, and Maria Antonietta Loi**

Hybrid perovskite solar cells have attracted an unprecedented research attention due to their skyrocketing record power conversion efficiency (PCE), which now exceeds 23% in less than a decade from the initial PCE of 3.8%. Besides the excellent optoelectronic properties of the perovskite absorbers, the high efficiencies are also dependent on preparation methods and advanced device engineering. In this study, the role of the device architecture (planar n-i-p vs inverted p-i-n structure) and of the charge-selective interlayer on the photophysical properties of the perovskite absorber and device performance are explored. $FA_{0.85}MA_{0.15}PbBr_{0.45}I_{2.55}$ (MA = methylammonium, FA = formamidinium) as the perovskite absorber and chloride-capped TiO_2 colloidal nanocrystals (TiO_2-Cl) and poly(3,4-ethylene dioxythiophene):poly(styrenes ulfonate) (PEDOT:PSS) as close-to-the-substrate layers in the conventional and inverted structures are employed, respectively. Extremely different device performances are demonstrated by the two structures. The device where the active layer is deposited on TiO_2-Cl displays a champion PCE of 19.9%, while the one using PEDOT:PSS gives about 15.1% efficiency. The photophysical and electrical investigations indicate that the TiO_2-Cl/perovskite interface has lower number of traps, underlining the importance of interfaces for achieving highly performing perovskite solar cells.

1. Introduction

In recent years, organic-inorganic metal halide perovskites have become one of the most promising intrinsic semiconductors for optoelectronic applications due to their ease of processing, low manufacturing cost, and exceptional photophysical properties. Some of the outstanding photophysical properties include high optical absorption coefficient, long charge carrier lifetimes, high carrier mobilities, long diffusion lengths, low trap densities, and broadly tunable bandgaps from the visible to the near-infrared.[1–4] Optoelectronic devices such as light-emitting diodes,[5–9] lasers,[5,10] light emitting field-effect transistors,[11] photodetectors,[12,13] and photovoltaics[14–22] have all been realized with many of them increasingly gaining intense research attention. In particular, organic-inorganic metal halide perovskite solar cells (PSCs) have for the past few years attracted an unprecedented interest due to their ever increasing record efficiency which now stands at a certified power conversion efficiency (PCE) of 23.7%[23] from the initial value of 3.8% recorded in 2009.[1]

The rapid advancements in perovskite photovoltaic (PV) research can generally be attributed to the quest to soon commercialize the technology by improving device efficiency and overcoming the major challenging issues that hinder these steps, such as the long-term device operational stability, the material toxicity, and the functioning instability (hysteresis). Efforts toward improving efficiency and mitigating the abovementioned crucial challenges have therefore led to various advancements that can be attributed to three primary factors: deposition methods, chemical engineering, device architecture engineering.[24] For instance, to achieve high-quality perovskite films with the right morphology, crystallinity, and phase purity, deposition techniques such as one-step solution deposition,[2,25] two-step solution deposition,[26,27] vapor-assisted solution deposition,[28] and thermal vapor deposition[29,30] methods have been developed. To further improve the perovskite film morphology, and crystallinity, solvent engineering (e.g., use of mixed-solvents and solvent additives),[22,31] anti-solvent treatment, solvent annealing and hot-casting,[22,32,33] have also been developed. The chemical engineering of the hybrid perovskite has been used to modify the bandgap[3,4] and increase the crystallographic and thermal stability of the active layer.[20]

Lastly, different device architectures have been utilized. Depending on which electrode is on the glass substrate or which charge-selective material is encountered first by the light, two primary device architectures can be classified: conventional (n-i-p)[2,34] and inverted[18,35,36] (p-i-n) device architectures. Thus, whereas in the conventional device architecture the electron-extracting electrode encounters the light first, in the inverted

S. Adjokatse, J. Kardula, Dr. H.-H Fang, Dr. S. Shao, G. H. ten Brink, Prof. M. A. Loi
Zernike Institute for Advanced Materials
University of Groningen
Nijenborgh 4, 9747 AG Groningen, The Netherlands
E-mail: m.a.loi@rug.nl

The ORCID identification number(s) for the author(s) of this article can be found under https://doi.org/10.1002/admi.201801667.

DOI: 10.1002/admi.201801667

device architecture, the hole-extracting electrode is the first. These device architectures can further be sub-categorized based on whether the perovskite absorber is infiltrated into a mesoporous material (mesoscopic device structure)[34,37,38] or sandwiched between an electron- and hole-selective material (planar device structure).[28,29,35,39]

In general, the performances of PSCs are known to be dependent on device architecture and although the excellent PCEs reported are not limited to any particular device configuration, most of the top-performing devices with PCEs above 20% are based on the conventional (both mesoscopic and planar) device architectures.[20,40] On the other hand, only very few high-performing devices based on the inverted architecture have been reported with the highest uncertified PCE been 19.4%, using poly(triaryl amine) (PTAA) as the close-to-the-substrate layer.[41] Although Momblona et al. were the first to directly compare the performance of opposite device configurations, their study was focused on the demonstration of fully vacuum deposited perovskite solar cells and also, the impact of p- and n-type doped organic semiconductor transport layers on device performance.[42] Thus, due to the excitement surrounding the rapidly increasing efficiencies, not much attention has been devoted to the fundamental study of the impact of the material on which the perovskite is deposited and device architecture on the device performances and the corresponding photophysics.

The composition of the perovskite plays a key role in the efficiency and stability of the devices. For instance, most of the PCEs above 17% which are certified are based on the (FA/MA)Pb(I/Br) (MA = methylammonium, FA = formamidinium) perovskite composition[23,43] and the (Cs/FA/MA)Pb(I/Br) system, which is shown to be much more stable.[20,43] It is also important to note that all these devices are fabricated based on the conventional device architecture. Hence, to examine the applicability and dependence of (FA/MA)Pb(I/Br) perovskite on the material on which the active layer is deposited and alternative device architecture, we fabricated inverted planar PSCs with the commonly used organic hole-selective material, PEDOT:PSS. Our champion device in this architecture reached a PCE of 15.1% with an average PCE of 12.2 ± 1.1%. For comparison, we fabricated devices based on conventional planar device architecture with identical processing of the perovskite absorber. The perovskite is deposited on chloride-capped TiO_2 (TiO_2-Cl) nanocrystals (NC) film,[40] a low temperature processed transport material which acts as electron-selective layer (ESL). In this architecture, champion PCE of 19.9% and an average PCE of 16.8 ± 1.2% is achieved. This extreme difference in performance compelled us to further investigate the morphological, structural and photophysical properties of the perovskite films and devices, in order to gain insight into the impact of the substrate material and the device architecture on the device performances. Our results show that TiO_2-Cl NC film serves as a better surface for the formation of a more compact and pinhole-free perovskite film than PEDOT:PSS. Additionally, we attribute the better performance of the conventional device to a lower number of traps at the interfaces with the extracting layers. Particularly the TiO_2-Cl/perovskite interface is shown to be much superior with respect to the PEDOT:PSS/perovskite interface. This underlines the importance of interfaces for achieving highly performing perovskite solar cells.

2. Results and Discussion

In this study, we fabricated mixed-cation mixed-halide perovskite solar cells based on two different planar device architectures (inverted p-i-n and conventional n-i-p) and investigate the effect of the layer on which the active material is deposited, from here thereof called substrate layer, and device structure on their PV performances. As shown in **Figure 1**a,b, our inverted p-i-n device has the structure ITO/PEDOT:PSS/$FA_{0.85}MA_{0.15}PbBr_{0.45}I_{2.55}$/PCBM/Al and the conventional n-i-p device has the structure ITO/TiO_2-Cl/$FA_{0.85}MA_{0.15}PbBr_{0.45}I_{2.55}$/Spiro-OMeTAD/Au. For these configurations, PEDOT:PSS and TiO_2-Cl NC films which serve as substrate layers in both structures are deposited on patterned ITO-coated glass, and act as the hole-selective and electron-selective contacts in the respective device architectures. PCBM and Spiro-OMeTAD are the electron-selective and hole-selective layers deposited before cathode and anode metals, respectively. The perovskite absorber and all the transport layers are deposited by spin-coating. The perovskite active layers are deposited for both device configurations using the anti-solvent technique with identical set of solvents and processing parameters to ensure fully optimized perovskite films on the different substrate layers.[22]

The current density–voltage (*J*–*V*) characteristics of the two types of devices under 1 Sun illumination are extremely different. The solar cells based on the regular device architecture are much better in performance than those based on the inverted device architecture. The *J*–*V* curves are reported in Figure 1c, with the corresponding PV parameters listed in **Table 1**. The best-performing regular device gives a PCE of 19.9% (short-circuit current density, J_{sc} of 25.3 mA cm^{-2}, open-circuit voltage, V_{oc} of 1.09 V, and fill factor, *FF* of 0.72). The best inverted devices, instead gives a PCE of 15.1% (J_{sc} of 19.2 mA cm^{-2}, V_{oc} of 0.96 V, *FF* of 0.82). To the best of our knowledge, this is the highest PCE recorded using PEDOT:PSS and PCBM as transport layers without any interface engineering and based on the inverted structure. Although the perovskite absorber in both type of devices is nominally identical, the PV metrics show an increase of both J_{sc} (from 19.2 to 25.3 mA cm^{-2}) and V_{oc} (from 0.96 to 1.09 V) in favor of the regular architecture. However, the *FF* shows an increase from 0.72 to 0.82 going from the regular to the inverted structure. The external quantum efficiency (EQE) spectra shown in Figure 1d also illustrate a vast difference in the light harvesting capabilities of the perovskite when used in the two different device architectures. Whereas the inverted device exhibits a broad plateau around 80% over the spectral range between 400 and 740 nm, the regular device shows a light harvesting ability of over 90% within the same spectral range. The calculated photocurrent densities are 18.8 and 23.0 mA cm^{-2}, respectively, which are slightly lower but reasonably in good agreement with the J_{sc} values obtained from the *J*–*V* curves.

Figure 2a,b displays the statistical performances measured for more than 30 inverted and more than 60 regular devices. Their average PV metrics are also given in 1 and Figure 2f displays the data in a box chart. The wider PCE distribution for the inverted devices with respect to the regular ones is mainly influenced by the very different J_{sc} distribution (Figure 2c) of the two device types. On the other hand, the other PV parameters show relatively

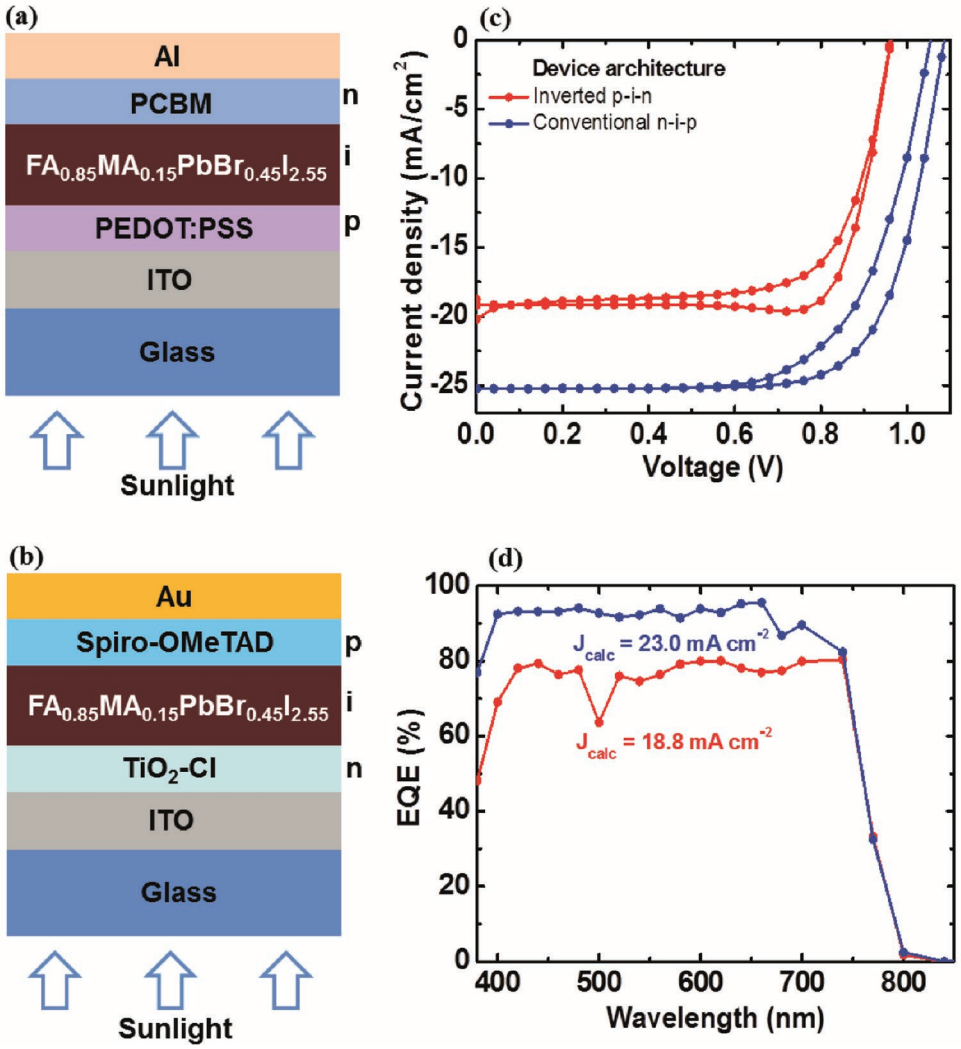

Figure 1. Device architecture and planar perovskite solar cells (PSCs) characteristics. Schematic diagrams of planar perovskite solar cells in a) inverted p-i-n configuration and b) conventional n-i-p configuration. c) *J–V* curves of PSCs in inverted p-i-n and conventional n-i-p device configuration. d) External quantum efficiency spectra of the devices reported in (c).

similar variation for the two structures (see Figure 2d,e, for the open-circuit voltage and fill factor, respectively). Interestingly, although the J_{sc} and V_{oc} show not only high reproducibility but also superior values, the major limiting factor to the performance of the regular devices is the fill factor.

Table 1. Solar cell performance parameters extracted from the reverse *J–V* curves in Figure 1c.

Architecture	J_{sc} [mA cm^{-2}]	V_{oc} [V]	FF	PCE [%]
Inverted p-i-n (Champion cell)	19.2	0.96	0.82	15.1
Inverted p-i-n (Average)	18.0 ± 1.2	0.88 ± 0.04	0.77 ± 0.05	12.2 ± 1.1
Regular n-i-p (Champion cell)	25.3	1.09	0.72	19.9
Regular n-i-p (Average)	25.0 ± 0.3	1.05 ± 0.03	0.65 ± 0.04	16.8 ± 1.2

To gain insight into why the different device architecture types with identically processed perovskite films exhibit extremely different device performances, we first examine the optical, structural, and morphological properties of the films when deposited on the different substrate layers. In general, high quality films with controlled morphology, high surface coverage, and minimum pinholes are required for high performing planar perovskite solar cells. And since these requirements are influenced by factors such as material composition, additives, deposition method, and film treatment, they are kept under control in the device fabrication process in order to obtain the identically processed perovskite films. Of course, the surface energy of the substrate layer will also have a large influence on the morphology of the active layer.

Figure 3a shows both the absorbance and normalized steady-state photoluminescence (PL) spectra of the perovskite films

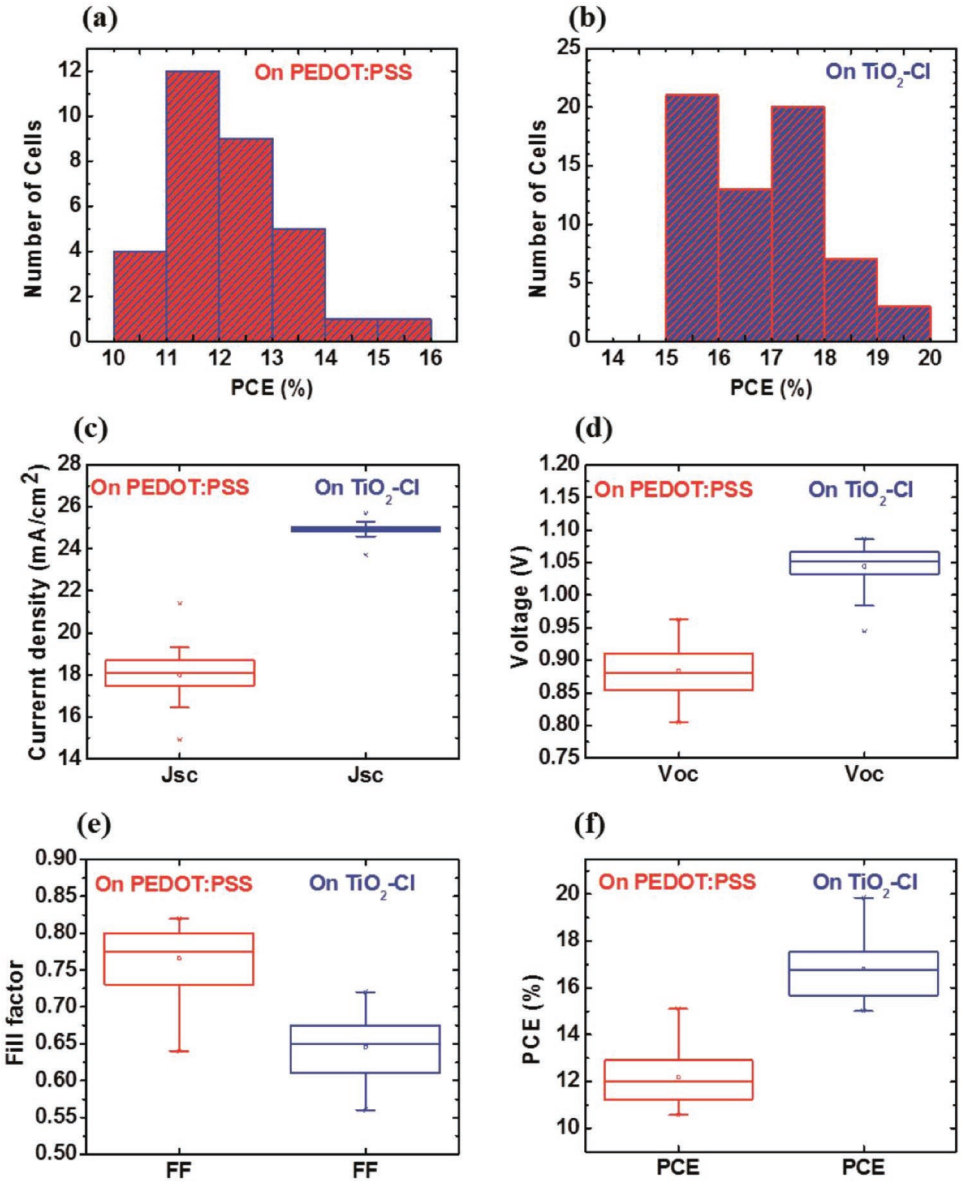

Figure 2. Statistical performance of the planar perovskite solar cells. Histogram of the PCE values of the devices with a) PEDOT:SSS and b) TiO_2-Cl as the substrate layer. Box chart of the PV metrics showing the comparison of the c) short-circuit current, d) open-circuit voltage, e) Fill factor, and f) PCE of the devices based on the inverted p-i-n and conventional n-i-p architectures.

deposited on PEDOT:PSS and TiO_2-Cl. While the identical absorbance spectra are indicative of the same thickness, the identical PL spectra show that both films exhibit identical compositional order. Similarly, the X-ray diffraction (XRD) pattern of the perovskite films on both substrate layers exhibit identical diffraction peaks with no traces of secondary phases (see Figure 3b). The peak intensities as well as the full width at half maximum (FWHM) are also identical, which is characteristic of identical structure and disorder. Figure 3c,d show the top-view scanning electron microscopy (SEM) images of the perovskite thin films formed on PEDOT:PSS and on Cl-capped TiO_2 films, respectively. The insets are higher magnification micrographs of the same thin films. Although the films exhibit high surface coverage on both surfaces, with identical grain sizes, the overall morphological quality is different. Whereas the perovskite film on the Cl-capped TiO_2-coated layer exhibits higher compactness with minimal occurrence of pinholes, the films deposited on PEDOT:PSS show a much higher number of pinholes and pronounced open grain boundaries which are known to be detrimental to device performance.[17] For example, the pinholes are likely to cause direct contact between the anode and cathode interfacial materials and therefore lead to high leakage current and thus shunt losses in the device. The grain boundaries induce Schottky defects and cause significant trap assisted recombination.[17,44,45] These conditions lead to higher charge recombination and directly affect both the V_{oc} and J_{sc}. Besides the macroscopic appearance of pinholes and the more open grains exhibited by the perovskites grown on PEDOT:PSS,

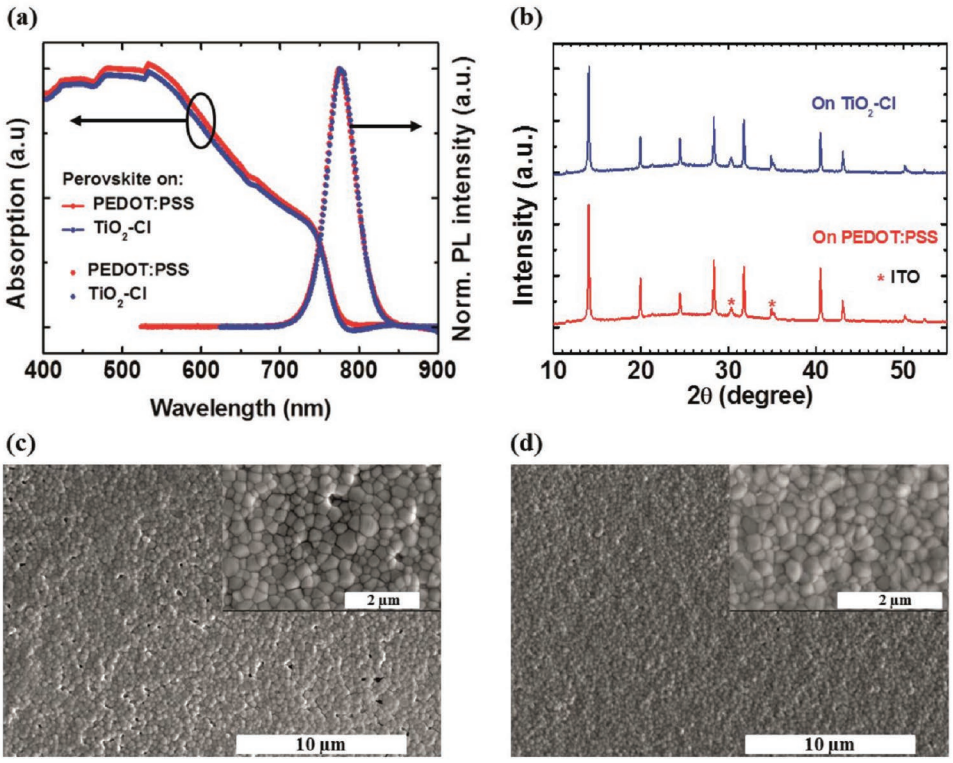

Figure 3. Optical, structural, and morphological characterization of perovskite film on PEDOT:PSS and TiO_2-Cl. a) Absorbance and photoluminescence spectra, b) XRD patterns, and c,d) top-view SEM images of $FA_{0.85}MA_{0.15}PbBr_{0.45}I_{2.55}$ thin film on PEDOT:PSS- and TiO_2-Cl-coated ITO substrates. The insets show higher magnification with scale bar of 2 μm.

the atomic force microscopy (AFM) micrographs show a root mean square (RMS) roughness of ≈11 nm for the perovskite film grown on PEDOT:PSS and ≈26 nm for the sample grown on TiO_2-Cl. The AFM micrographs from which these roughness values are obtained are shown in Figure S1, Supporting Information. We believe that this difference in roughness could be induced by the different morphology of the underlying substrate layers.

Effective PL quenching of the perovskite emission by the charge transport materials and consequently, a shorter PL decay lifetime can be considered as an indicator for effective charge transfer. It can also give insight into the charge recombination dynamics at the perovskite/ESL(HSL) interfaces and in eventual trapping of the photoexcited charge carriers. Hence, we employ steady-state PL and time-resolved photoluminescence (TRPL) spectroscopy to investigate the charge transfer kinetics between the perovskite films and the transport layers. To avoid selective interrogation, the samples are photo-excited from both the glass (bottom layer) and the film sides (top layer). The data obtained for excitations from the glass side are similar to those obtained from the film side and are indicative of the degree of the charge recombination, charge trapping, or the effectiveness of charge extraction by the charge selective layers. The steady-state PL and TRPL response of the perovskite films coated on/below the n- and p-type transport materials are shown in **Figure 4**. Among the n-type materials, PCBM shows stronger PL quenching than the TiO_2-Cl NC film (Figure 4a), while among the p-type transport layers, both PEDOT:PSS and Spiro-OMeTAD exhibit similar PL quenching capabilities (Figure 4b). This observation is consistent with the previous work by Snaith and coworkers where they showed that the PL quenching of $CH_3NH_3PbI_{3-x}Cl_x$ perovskite emission by n-type quenchers such as high-temperature sintered sol-gel TiO_2 and PCBM and the p-type quenchers follow the same trend.[39] On the other hand, Tan et al. demonstrated an effective PL quenching by the colloidal nanocrystal-based films of TiO_2 and TiO_2-Cl to a similar degree which they attributed to excellent band alignment and fast charge extraction by these transport materials.[40]

It is important to underline that a strong quenching does not automatically correlate to an effective extraction of charge carrier and therefore to good solar cells performance. Recently, we have shown the comparison of two different fullerene derivatives for which the PL quenching and the device performance did not correlate with each other. This was attributed to the fact that trapping of charge carriers also reduces the effective PL intensity.[16]

The corresponding PL decays for the n- and p-type transport materials are shown in Figure 4c,d, respectively. The decay profiles are fitted with bi-exponential functions, exhibiting fast (τ_1) and slow (τ_2) decay lifetimes. The perovskite film on the ITO-coated glass has a fast decay lifetime (τ_1) of 54.7 ns and a slow decay lifetime (τ_2) of 170.4 ns. When the perovskite films are interfaced with PEDOT:PSS, the PL decay becomes overall faster with a first component with lifetime τ_1 = 3.2 ns and the second component of τ_2 = 53.5 ns. For the interface with Spiro-OMeTAD, the measured lifetimes are τ_1 = 5.5 ns and τ_2 = 16.5 ns. When considering the average decay lifetimes, the interface with Spiro-OMeTAD has a much shorter lifetime of

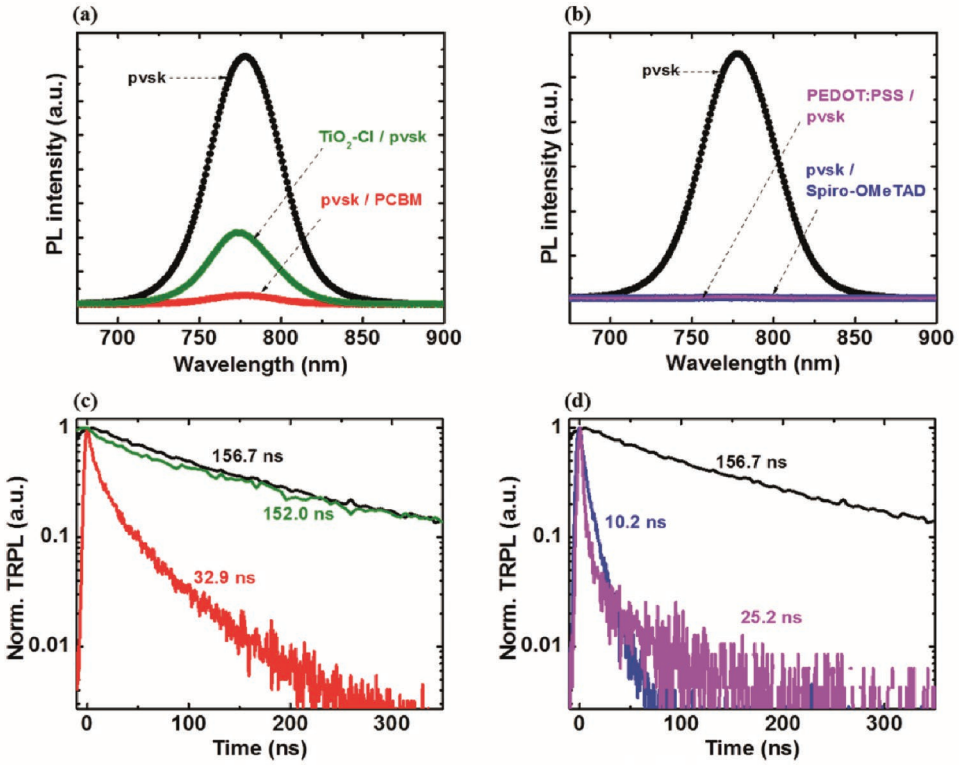

Figure 4. Photoluminescence response of $FA_{0.85}MA_{0.15}PbBr_{0.45}I_{2.55}$ perovskite films coated on/with n- and p-type quenchers. a) Steady-state photoluminescence spectra of n-type quenchers and b) p-type quenchers of perovskite films processed in a bi-layer configuration. c) Corresponding time-resolved photoluminescence decay of perovskite thin films for n-type quenchers and d) p-type quenchers. The excitation was performed from both the glass and the side of the deposited layers.

τ_{avg} = 10.2 ns, than that of the PEDOT:PSS interface of 25.2 ns. On the other hand, the rate of electron extraction by PCBM and TiO_2-Cl is clearly distinguished. PCBM gives a shorter average lifetime of 32.9 ns, while the average PL lifetime of the perovskite film on TiO_2-Cl NC film is 152.0 ns, which is comparable to that on ITO-coated glass, 156.7 ns. Therefore, the significant PL quenching by the TiO_2-Cl NC film does not correlate with the observed long decay lifetime, implying that either the extraction of the electrons occur at a faster timescale beyond the resolution of the measuring instrument or that the TiO_2-Cl NC film is after all a poor electron extraction layer. Clearly, the excellent PV performances of the devices based on the TiO_2-Cl NC films allow us to exclude the latter reasoning. It is however important to emphasize again that a fast decay could also be due to trapping of the photoexcited charge carriers at the interface, as discussed above.[16]

To gain deeper understanding of the charge recombination mechanisms in the solar cells, light intensity dependent *J*–*V* characteristics are investigated. The dependence of the current density (*J*) on applied voltage (*V*) can be expressed using the Shockley diode equation

$$J = J_0\left[\exp\left(\frac{qV}{nkT}\right)-1\right]-J_{sc} \quad (1)$$

where J_0 is the reverse saturation current density, q is the elementary charge, n is the ideality factor, k is the Boltzmann's constant, and T is the temperature. At open circuit conditions (J = 0), the above equation can be rearranged to show the dependence of V_{oc} on illumination intensity (I),

$$V_{oc} = \frac{nkT}{q}\ln\left(\frac{J_{sc}}{J_0}\right) = \frac{nkT}{q}\ln\left(I^{\alpha}\right)+c \quad (2)$$

where c is a constant that takes into account all the terms that are independent of light intensity and α is an empirical parameter which determines the linearity of the photocurrent with light intensity. The empirical parameter (α) is unity for ideal devices. Similarly, the ideality factor (n) gives insight into the dominant recombination mechanisms in solar cells. Devices with dominant bimolecular recombination have ideality factor close to unity while those with dominant trap-assisted recombination have values close to 2.

The *J*–*V* characteristics of the two types of devices for illumination intensities ranging from 3.2 to 100 mW cm^{-2} are shown in Figure S2a,b, Supporting Information, respectively. The variation of the J_{sc} as a function of the illumination intensity is plotted on a log-log scale (Figure S2c, Supporting Information) and fitted with the power law $J_{sc} \propto I^{\alpha}$. The α values extracted are 0.94 and 1.00 for devices using PEDOT:PSS and TiO_2-Cl NC films, respectively. These values imply that bimolecular recombination is negligible in these devices at V = 0. Figure S2d, Supporting Information, also shows the dependence of V_{oc} on the light intensity from which the ideality factor n is extracted.

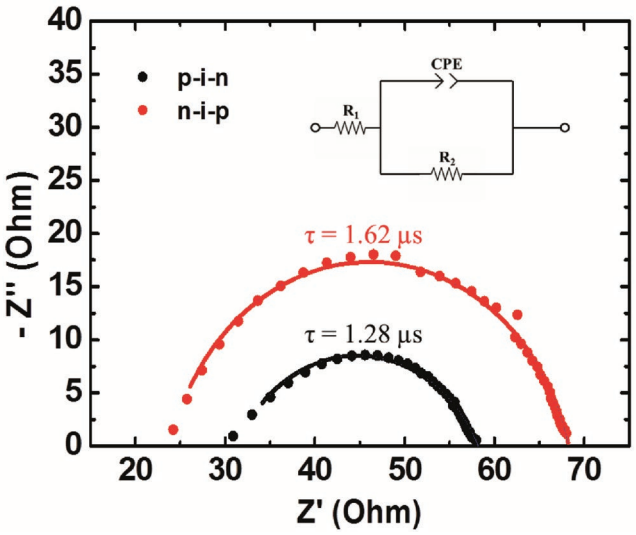

Figure 5. Impedance spectroscopy measurements under 1 Sun illumination at open circuit conditions. The inset shows the equivalent circuit used for the analysis. The circuit consists of a series resistance R_1, a constant phase element (CPE), and a recombination resistance R_2.

The ideality factor for the PEDOT:PSS-based and TiO_2-Cl NC film-based solar cells are calculated to be 1.55 and 1.49, respectively. This indicates that, both bimolecular and trap-assisted recombinations are present in these devices. The dominant trap-assisted charge recombination effect in the p-i-n device compared to the n-i-p device is in agreement with the observed performance of the devices and previous studies where it was shown that devices based on compact perovskite films exhibited less trap-assisted recombination and better *J–V* characteristics than noncompact perovskite films with open grain boundaries.[17] Hence, the differences in the *J–V* characteristics and particularly, the low V_{oc} and low J_{sc} observed in the p-i-n device can directly be attributed to higher rate of trap-assisted charge recombination as also demonstrated by Tvingstedt et al. and Shekar et al.[44,46]

To elucidate the effect of the interfaces on the performance of the devices and determine the recombination rate of charge carriers at the interfaces, impedance spectroscopic is performed. The impedance spectra of the n-i-p and p-i-n devices shown in **Figure 5**, were recorded under one sun illumination at open circuit condition. The equivalent circuit consisting of series resistance R_1, constant phase element (CPE), and recombination resistance R_2 as shown in the inset of Figure 5 is used to fit the Nyquist plot. The fitting parameters are shown in Table S1, Supporting Information. The characteristic lifetime τ of the charge carriers in the devices is obtained from the product of the recombination resistance and the chemical capacitance given by $C_2 = Q_2 (2\pi f_{peak})^{a-1}$ (i.e., $\tau = R_2C_2$) where f_{peak} is the frequency at the maximum imaginary component of the Nyquist spectrum, *a* indicates the deviation from an ideal capacitor, and Q is the constant phase element value. The Nyquist plot of the p-i-n device shows severely depressed semicircle with *a* value much lower than unity (0.72), which is indicative of significant inhomogeneity that is probably due to the pinholes and open grain boundaries in the perovskite film, which are responsible for significant trap-assisted charge recombination in the device. On the other hand, the n-i-p device displays almost perfect semicircle and behaves like a pure capacitor with *a* value close to unity (0.95). This is an indication of the homogeneity of the device, which is in good agreement with the compactness of the perovskite film observed in the SEM investigation (Figure 3d). The charge carriers in the p-i-n device have a shorter lifetime of about 1.2 µs due to charge recombination at the interfaces, while those in n-i-p device have a lifetime of about 1.6 µs implying a lower amount of traps at the interfaces.

Therefore, by correlating the electrical performance of the devices to the spectroscopic study, we can deduce that the effective PL quenching by the transport layers and the decay lifetimes are not entirely indicative of effective charge transfer between the perovskite films and the charge selective materials. Which means that, the shorter decay lifetime and the corresponding poor performance of the inverted p-i-n devices can be attributed to the presence of higher number of interface traps leading to charge carrier recombination. Interestingly, the better performance of the conventional n-i-p device confirms the effective trap passivation at the TiO_2-Cl/perovskite interface as proposed earlier by Tan et al.[40]

3. Conclusion

In summary, we studied the effect of the device architecture on the performance of $FA_{0.85}MA_{0.15}PbBr_{0.45}I_{2.55}$ planar perovskite solar cells. The inverted p-i-n and conventional n-i-p device architectures were fabricated, using PEDOT:PSS and Cl-capped TiO_2 as close-to-substrate/transport layers, respectively. The power conversion efficiency of the top-performing device based on the Cl-capped TiO_2 is 19.9%, which is much higher than the efficiency of about 15.1% obtained for the best device based on the p-i-n structure with PEDOT:PSS as substrate layer. To understand the extreme difference in device performances, we have investigated the dependence of structural and morphological properties of the $FA_{0.85}MA_{0.15}PbBr_{0.45}I_{2.55}$ perovskite thin films on the nature of the under layers. We find that the perovskite films formed on the Cl-capped TiO_2 NC layer are more compact and homogeneous with no, or minimum pinholes in comparison with the perovskite films on the PEDOT:PSS. X-ray diffraction characteristics show that the perovskite films are structurally identical. The photoluminescence and impedance spectroscopy measurements show that a lower amount of traps are present at the TiO_2-Cl/perovskite and perovskite/Spiro-OMeTAD interfaces than at the PEDOT:PSS/perovskite and perovskite/PCBM interfaces. Thus, the work presented here underlines the importance of device architecture and interfaces for achieving highly performing perovskite solar cells.

4. Experimental Section

Materials: Materials for the synthesis, cleaning, and preparation of colloidal solution of TiO_2 nanocrystals include titanium (IV) chloride ($TiCl_4$) (99.9% Sigma-Aldrich), absolute ethanol, benzyl alcohol, diethyl ether, anhydrous methanol, and anhydrous chloroform that were acquired from Sigma-Aldrich. PEDOT:PSS (Clevios VP Al 4083) water dispersion was acquired from Heraeus. The perovskite precursors: lead (II) iodide

(PbI_2) (99.99%), lead (II) bromide ($PbBr_2$), methylamine hydrobromide (MABr) (>98%), and formamidine hydroiodide (FAI) (>98%) were purchased from TCI EUROPE N.V. *N,N′*- Dimethylformamide (DMF) (99.8%), and Dimethyl sulfoxide (DMSO) (99.9%, Alfa Aesar) and all other materials were acquired from Sigma-Aldrich. All the materials were used as received without further purification.

The synthesis of the Cl-capped TiO_2 (TiO_2-Cl) nanocrystals and the perovskite precursor solution were prepared following previously reported work by Tan et al.[40] with little or no modification.

Film and Device Fabrication: Films and devices were fabricated on pre-patterned indium tin oxide (ITO) coated glass substrates, which were ultrasonically cleaned in detergent solution, deionized water, acetone, and isopropanol, sequentially. After drying them in an oven at 140 °C for about 10 min, they were treated with ultraviolet ozone (UV-O_3) for 20 min. The PEDOT:PSS and the TiO_2-Cl films were deposited onto the substrates by spin coating in ambient conditions at the speed of 3000 and 4000 rpm, respectively. The PEDOT:PSS films were dried at 140 °C for 10 min in an oven while the TiO_2-Cl films were dried at 150 °C for 30 min on a hotplate. The thicknesses of the obtained PEDOT:PSS and the TiO_2-Cl films were about 45 and 20 nm, respectively. The substrates were transferred into a nitrogen-filled glovebox immediately after cooling for further processing. The $FA_{0.85}MA_{0.15}PbBr_{0.45}I_{2.55}$ perovskite solution was prepared following the recipe described in[40] and stirred overnight at room temperature. The molar ratio of (FAI + MABr) and (PbI_2 + $PbBr_2$) was 1:1, dissolved in a mixed solvent of DMF and DMSO at a volume ratio of 4:1 to form a precursor solution of 1.2 M in concentration. The $FA_{0.85}MA_{0.15}PbBr_{0.45}I_{2.55}$ perovskite films were deposited by a one-step spin coating method involving a two-step spin program with anti-solvent (chlorobenzene) treatment. The spin program was set at 1000 rpm for 10 s and 4000 rpm for 30 s with the anti-solvent dripped at about 2–10 s prior to the end of the spinning. The variation in the anti-solvent dripping time is to aid in the optimization of the perovskite morphology while maintaining the same film thickness. The films were immediately annealed at 100 °C for 10 min. For the inverted devices, [60]PCBM dissolved in chlorobenzene at a concentration of 20 mg mL^{-1} was spin coated on the perovskite layer at 1500 rpm while for the conventional devices, 70 mg of Spiro-OMeTAD, 20 µL of tert-butylpyridine and 70 µL of bis(trifluoromethane)sulfonimide lithium (Li-TFSI) salt (170 mg mL^{-1} in acetonitrile) dissolved in 1 mL of chlorobenzene was spin coated at 3000 rpm. To complete the devices, 100 nm of Al and 80 nm of Au contacts were deposited on the [60]PCBM and Spiro-OMeTAD layers, respectively, by thermal evaporation under high vacuum (<10^{-7} mbar).

Solar Cell Characterization: The current density-voltage (*J–V*) characteristics of the solar cells were measured under simulated AM 1.5 solar illumination using an Osram HMI 1200W/DXS lamp in a nitrogen filled glovebox. The light intensity was calibrated to give 100 mW cm^{-2} using calibrated silicon reference cell (SRC-1000-RTD-QZ, VSLI Standards Inc.). The *J–V* curves were recorded using Keithley 2400 source-meter. The active area of the solar cells was defined with a metal aperture mask of 0.1 cm^2. Light intensity dependence measurements were performed using a set of neutral density filters to attenuate the illumination intensity. The temperature of the solar cell was controlled by an adjustable N_2 gas flow through a liquid N_2 bath.

The external quantum efficiency (EQE) measurements were carried out under short-circuit conditions using monochromatic light from 250 W quartz tungsten halogen lamp (Osram 64 655 HLX). A set of band pass filters with full width at half maximum (FWHM) of 10 ± 2 nm were used to obtain the monochromatic light.

Impedance spectroscopy measurements were performed using an SP-200 Bio-Logic potentiostat with a forward bias superimposed with a 25 mV AC perturbation over the frequency range 1 MHz–100 Hz.

Morphological Characterization: The SEM images were obtained using the FEI Nova Nano SEM 650 with an accelerating voltage of 5 kV while the AFM images were taken using the Bruker NanoScope V in ScanAsyst mode.

Structural and Optical Characterizations: The X-ray diffraction experiment was performed at ambient conditions using a Bruker D8 Advanced diffractometer in Bragg-Brentano geometry and operating with Cu Kα radiation source (λ = 1.54 Å) and Lynxeye detector.

The photoluminescence measurements were performed using the second harmonic (400 nm) of a Ti:sapphire laser (repetition rate, 76 MHz; Mira 900, Coherent) to excite the samples. The illumination power density was decreased to 5 µJ cm^{-2} by using a neutral density filter. The excitation beam was spatially limited by an iris and focused with a 150-mm focal length lens. Emitted photons were collected with a lens and directed to a spectrograph. For the time-resolved photoluminescence measurement, a pulse picker was used to divide the Ti:sapphire oscillator frequency (about 76 MHz). Steady-state spectra were collected using a Hamamatsu EM-CCD camera and time resolved traces were recorded using a Hamamatsu streak camera.

Supporting Information

Supporting Information is available from the Wiley Online Library or from the author.

Acknowledgements

The authors would like to acknowledge the technical support provided by Arjen Kamp and Teodor Zaharia. S.A. acknowledges financial support from The Netherlands Organization for Scientific Research (NWO Graduate Programme 2013, No. 022.005.006). The authors would also like to acknowledge funding from the European Research Council (ERC Starting Grant "Hy-SPOD" No. 306983) and the Foundation for Fundamental Research on Matter (FOM), which is part of the Netherlands Organization for Scientific Research (NWO), under the framework of the FOM Focus Group "Next Generation Organic Photovoltaics."

Conflict of Interest

The authors declare no conflict of interest.

Keywords

device structures, hybrid perovskites, interfaces, photoluminescence

Received: October 22, 2018
Revised: January 16, 2019
Published online: February 4, 2019

[1] A. Kojima, K. Teshima, Y. Shirai, T. Miyasaka, *J. Am. Chem. Soc.* **2009**, *131*, 6050.
[2] M. M. Lee, J. Teuscher, T. Miyasaka, T. N. Murakami, H. J. Snaith, *Science* **2012**, *338*, 643.
[3] J. H. Noh, S. H. Im, J. H. Heo, T. N. Mandal, S. Il Seok, *Nano Lett.* **2013**, *13*, 1764.
[4] G. E. Eperon, S. D. Stranks, C. Menelaou, M. B. Johnston, L. M. Herz, H. J. Snaith, *Energy Environ. Sci.* **2014**, *7*, 982.
[5] G. Xing, N. Mathews, S. S Lim, N. Yantara, X. Liu, D. Sabba, M. Grätzel, S. Mhaisalkar, T. C. Sum, *Nat. Mater.* **2014**, *13*, 476.
[6] J. Wang, N. Wang, Y. Jin, J. Si, Z. K. Tan, H. Du, L. Cheng, X. Dai, S. Bai, H. He, Z. Ye, M. L. Lai, R. H. Friend, W. Huang, *Adv. Mater.* **2015**, *27*, 2311.
[7] H. Cho, S.-H. Jeong, M.-H. Park, Y.-H. Kim, C. Wolf, C.-L. Lee, J. H. Heo, A. Sadhanala, N. Myoung, S. Yoo, S. H. Im, R. H. Friend, T.-W. Lee, *Science* **2015**, *350*, 1222.

[8] A. Sadhanala, S. Ahmad, B. Zhao, N. Giesbrecht, P. M. Pearce, F. Deschler, R. L. Z. Hoye, K. C. Gödel, T. Bein, P. Docampo, S. E. Dutton, M. F. L. De Volder, R. H. Friend, *Nano Lett.* **2015**, *15*, 6095.
[9] Z.-K. Tan, R. S. Moghaddam, M. L. Lai, P. Docampo, R. Higler, F. Deschler, M. Price, A. Sadhanala, L. M. Pazos, D. Credgington, F. Hanusch, T. Bein, H. J. Snaith, R. H. Friend, *Nat. Nanotechnol.* **2014**, *9*, 1.
[10] F. Deschler, M. Price, S. Pathak, L. E. Klintberg, D. D. Jarausch, R. Higler, S. Hüttner, T. Leijtens, S. D. Stranks, H. J. Snaith, M. Atatüre, R. T. Phillips, R. H. Friend, *J. Phys. Chem. Lett.* **2014**, *5*, 1421.
[11] X. Y. Chin, D. Cortecchia, J. Yin, A. Bruno, C. Soci, *Nat. Commun.* **2015**, *6*, 1.
[12] R. Dong, Y. Fang, J. Chae, J. Dai, Z. Xiao, Q. Dong, Y. Yuan, A. Centrone, X. C. Zeng, J. Huang, *Adv. Mater.* **2015**, *27*, 1912.
[13] Y. Fang, Q. Dong, Y. Shao, Y. Yuan, J. Huang, *Nat. Photonics* **2015**, *9*, 679.
[14] N. J. Jeon, J. H. Noh, W. S. Yang, Y. C. Kim, S. Ryu, J. Seo, S. Il Seok, *Nature* **2015**, *517*, 476.
[15] S. Shao, Z. Chen, H.-H. Fang, G. H. Ten Brink, D. Bartesaghi, S. Adjokatse, L. J. A. Koster, B. J. Kooi, A. Facchetti, M. A. Loi, *J. Mater. Chem. A* **2015**, *4*, 2419.
[16] S. Shao, M. Abdu-Aguye, L. Qiu, L.-H. Lai, J. Liu, S. Adjokatse, F. Jahani, M. E. Kamminga, G. H. ten Brink, T. T. M. Palstra, B. J. Kooi, J. C. Hummelen, M. Antonietta Loi, *Energy Environ. Sci.* **2016**, *9*, 2444.
[17] S. Shao, M. Abdu-Aguye, T. S. Sherkar, H.-H. Fang, S. Adjokatse, G. ten Brink, B. J. Kooi, L. J. A. Koster, M. A. Loi, *Adv. Funct. Mater.* **2016**, *26*, 8094.
[18] B. G. H. M. Groeneveld, M. Najafi, B. Steensma, S. Adjokatse, H.-H. Fang, F. Jahani, L. Qiu, G. H. ten Brink, J. C. Hummelen, M. A. Loi, *APL Mater.* **2017**, *5*, 076103.
[19] H. Tsai, W. Nie, J.-C. Blancon, C. C. Stoumpos, R. Asadpour, B. Harutyunyan, A. J. Neukirch, R. Verduzco, J. J. Crochet, S. Tretiak, L. Pedesseau, J. Even, M. A. Alam, G. Gupta, J. Lou, P. M. Ajayan, M. J. Bedzyk, M. G. Kanatzidis, A. D. Mohite, *Nature* **2016**, *536*, 312.
[20] M. Saliba, T. Matsui, J.-Y. Seo, K. Domanski, J.-P. Correa-Baena, N. Mohammad K., S. M. Zakeeruddin, W. Tress, A. Abate, A. Hagfeldt, M. Grätzel, *Energy Environ. Sci.* **2016**, *9*, 1989.
[21] M. Saliba, T. Matsui, K. Domanski, J.-Y. Seo, A. Ummadisingu, S. M. Zakeeruddin, J.-P. Correa-Baena, W. R. Tress, A. Abate, A. Hagfeldt, M. Gratzel, *Science* **2016**, *354*, 206.
[22] N. J. Jeon, J. H. Noh, Y. C. Kim, W. S. Yang, S. Ryu, S. Il Seok, *Nat. Mater.* **2014**, *13*, 1.
[23] Research Cell Efficiency Records. National Renewable Energy Laboratory. https://www.nrel.gov/pv/assets/pdfs/pv-efficiency-chart.20181214.pdf, accessed: January 2019.
[24] Z. Song, S. C. Watthage, A. B. Phillips, M. J. Heben, *J. Photonics Energy* **2016**, *6*, 022001.
[25] N. Ahn, D.-Y. Son, I.-H. Jang, S. M. Kang, M. Choi, N.-G. Park, *J. Am. Chem. Soc.* **2015**, *137*, 8696.
[26] J. Burschka, N. Pellet, S.-J. Moon, R. Humphry-Baker, P. Gao, M. K. Nazeeruddin, M. Grätzel, *Nature* **2013**, *499*, 316.
[27] Z. Xiao, C. Bi, Y. Shao, Q. Dong, Q. Wang, Y. Yuan, C. Wang, Y. Gao, J. Huang, *Energy Environ. Sci.* **2014**, *7*, 2619.
[28] Q. Chen, H. Zhou, Z. Hong, S. Luo, H.-S. Duan, H.-H. Wang, Y. Liu, G. Li, Y. Yang, *J. Am. Chem. Soc.* **2014**, *136*, 622.
[29] M. Liu, M. B. Johnston, H. J. Snaith, *Nature* **2013**, *501*, 395.
[30] C.-W. Chen, H.-W. Kang, S.-Y. Hsiao, P.-F. Yang, K.-M. Chiang, H.-W. Lin, *Adv. Mater.* **2014**, *26*, 6647.
[31] J. A. Love, S. D. Collins, I. Nagao, S. Mukherjee, H. Ade, G. C. Bazan, T. Q. Nguyen, *Adv. Mater.* **2014**, *26*, 7308.
[32] Z. Xiao, Q. Dong, C. Bi, Y. Shao, Y. Yuan, J. Huang, *Adv. Mater.* **2014**, *26*, 6503.
[33] W. Nie, H. Tsai, R. Asadpour, J.-C. Blancon, A. J. Neukirch, G. Gupta, J. J. Crochet, M. Chhowalla, S. Tretiak, M. A. Alam, H.-L. Wang, A. D. Mohite, *Science* **2015**, *347*, 522.
[34] H.-S. Kim, C.-R. Lee, J.-H. Im, K.-B. Lee, T. Moehl, A. Marchioro, S.-J. Moon, R. Humphry-Baker, J.-H. Yum, J. E. Moser, M. Grätzel, N.-G. Park, *Sci. Rep.* **2012**, *2*, 591.
[35] J.-Y. Jeng, Y.-F. Chiang, M.-H. Lee, S.-R. Peng, T.-F. Guo, P. Chen, T.-C. Wen, *Adv. Mater.* **2013**, *25*, 3727.
[36] Q. Wang, Y. Shao, Q. Dong, Z. Xiao, Y. Yuan, J. Huang, *Energy Environ. Sci.* **2014**, *7*, 2359.
[37] T. Leijtens, G. E. Eperon, S. Pathak, A. Abate, M. M. Lee, H. J. Snaith, *Nat. Commun.* **2013**, *4*, 2885.
[38] J. H. Heo, S. H. Im, J. H. Noh, T. N. Mandal, C.-S. Lim, J. A. Chang, Y. H. Lee, H. Kim, A. Sarkar, M. K. Nazeeruddin, M. Grätzel, S. Il Seok, *Nat. Photonics* **2013**, *7*, 486.
[39] P. Docampo, J. M. Ball, M. Darwich, G. E. Eperon, H. J. Snaith, *Nat. Commun.* **2013**, *4*, 2761.
[40] H. Tan, A. Jain, O. Voznyy, X. Lan, F. Pelayo García De Arquer, J. Z. Fan, R. Quintero-Bermudez, M. Yuan, B. Zhang, Y. Zhao, F. Fan, P. Li, L. N. Quan, Y. Zhao, Z.-H. Lu, Z. Yang, S. Hoogland, E. H. Sargent, *Science* **2017**, *355*, 722.
[41] Y. Shao, Y. Yuan, J. Huang, *Nat. Energy* **2016**, *1*, 15001.
[42] C. Momblona, L. Gil-Escrig, E. Bandiello, E. M. Hutter, M. Sessolo, K. Lederer, J. Blochwitz-Nimoth, H. J. Bolink, *Energy Environ. Sci.* **2016**, *9*, 3456.
[43] L. K. Ono, E. J. Juarez-Perez, Y. Qi, *ACS Appl. Mater. Interfaces* **2017**, *9*, 30197.
[44] T. S. Sherkar, C. Momblona, L. Gil-Escrig, J. Ávila, M. Sessolo, H. J. Bolink, L. J. A. Koster, *ACS Energy Lett.* **2017**, *2*, 1214.
[45] Z. Chu, M. Yang, P. Schulz, D. Wu, X. Ma, E. Seifert, L. Sun, X. Li, K. Zhu, K. Lai, *Nat. Commun.* **2017**, *8*, 2230.
[46] K. Tvingstedt, L. Gil-Escrig, C. Momblona, P. Rieder, D. Kiermasch, M. Sessolo, A. Baumann, H. J. Bolink, V. Dyakonov, *ACS Energy Lett.* **2017**, *2*, 424.